Supplementary Information

Helical dislocation-driven plasticity and flexible high-performance thermoelectric generator in α-Mg_3Bi_2 single crystals

Mingyuan Hu[1, 2]†, Jianmin Yang[1]†, Yan Wang[1]†, Junchao Xia[1,3], Quan Gan[1], Shuhuan Yang[1,3], Juping Xu[4], Shulin Liu[4], Wen Yin[4], Baohai Jia[1], Lin Xie[1], Haifeng Li[3], and Jiaqing He[1, 2*]

[1]Shenzhen Key Laboratory of Thermoelectric Materials, Department of Physics, Southern University of Science and Technology, Shenzhen, 518055, China.

[2]Guangdong Provincial Key Laboratory of Advanced Thermoelectric Materials and Device Physics, Southern University of Science and Technology, Shenzhen 518055, China.

[3]Institute of Applied Physics and Materials Engineering, University of Macau, Avenida da Universidade, Taipa, Macao SAR, 999078, China.

[4]Spallation Neutron Source Science Center, Dongguan 523803, China.

†These authors contributed equally to this work.

[*]Correspondence to：hejq@sustech.edu.cn **(J.Q.H.)**

Contents:

Supplementary Note 1

Equations of carrier transport properties

The carrier transport properties of thermoelectric materials mainly include σ and S. According to Boltzmann transport theory, in the single parabolic band model, the σ can generally be obtained by the following formula[76,77]:

$$\sigma = ne\mu \tag{1}$$

where μ is Hall mobility, which is $\mu = \frac{e\tau}{m^*}$, where τ is carrier relaxation time and m^* is density of states effective mass.

The S of a metal and a degenerate semiconductor (heavily doped semiconductor, whose carrier concentration generally exceeds 10^{19} cm^{-3}) can be expressed as:

$$S = \frac{8\pi^2 k_B^2 m^* T}{3eh^2}\left(\frac{\pi}{3n}\right)^{2/3} \tag{2}$$

where k_B is the Boltzmann constant, e is the charge of the electron, h is the Planck constant, n is the carrier concentration.

Supplementary Section 1: Phase and Mechanical performance for α-Mg_3Bi_2 crystals.

Supplementary Figure 1. The as-grown p-type α-Mg_3Bi_2 crystal.

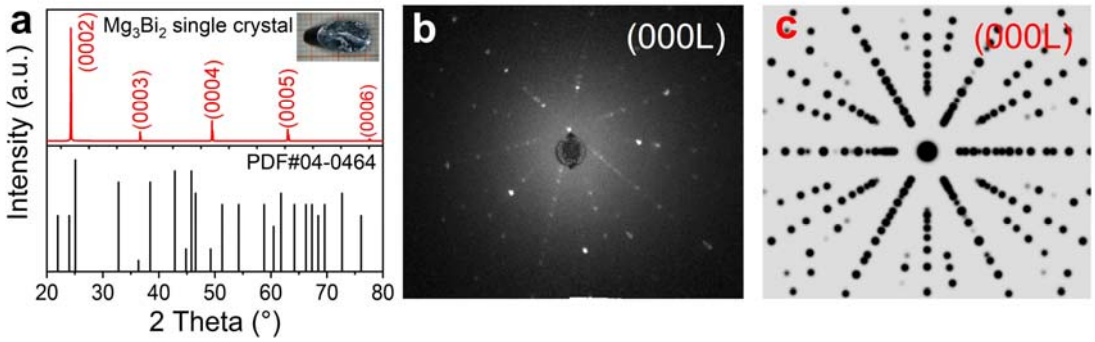

Supplementary Figure 2. Single crystal' XRD and Laue diffraction patterns of *α*-Mg_3Bi_2. a, XRD pattern for cleavage *α*-Mg_3Bi_2 crystal, showing the (000L) facet. **b**, Obtained Laue diffraction pattern in experiment, which matched with the calculated Laue diffraction pattern (**c**).

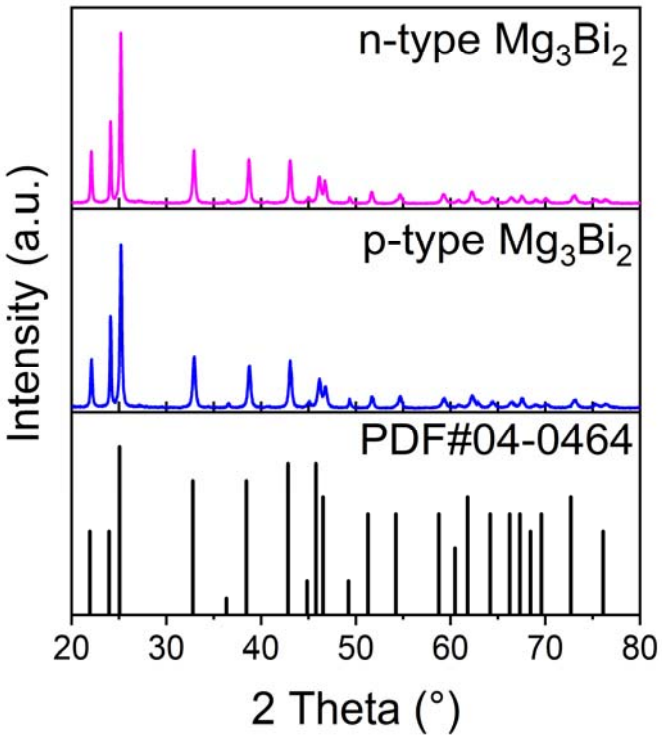

Supplementary Figure 3. Powder XRD patterns for n-type and p-type α-Mg_3Bi_2 crystals, which matched with the PDF#04-0464 card, meaning there were no second phase.

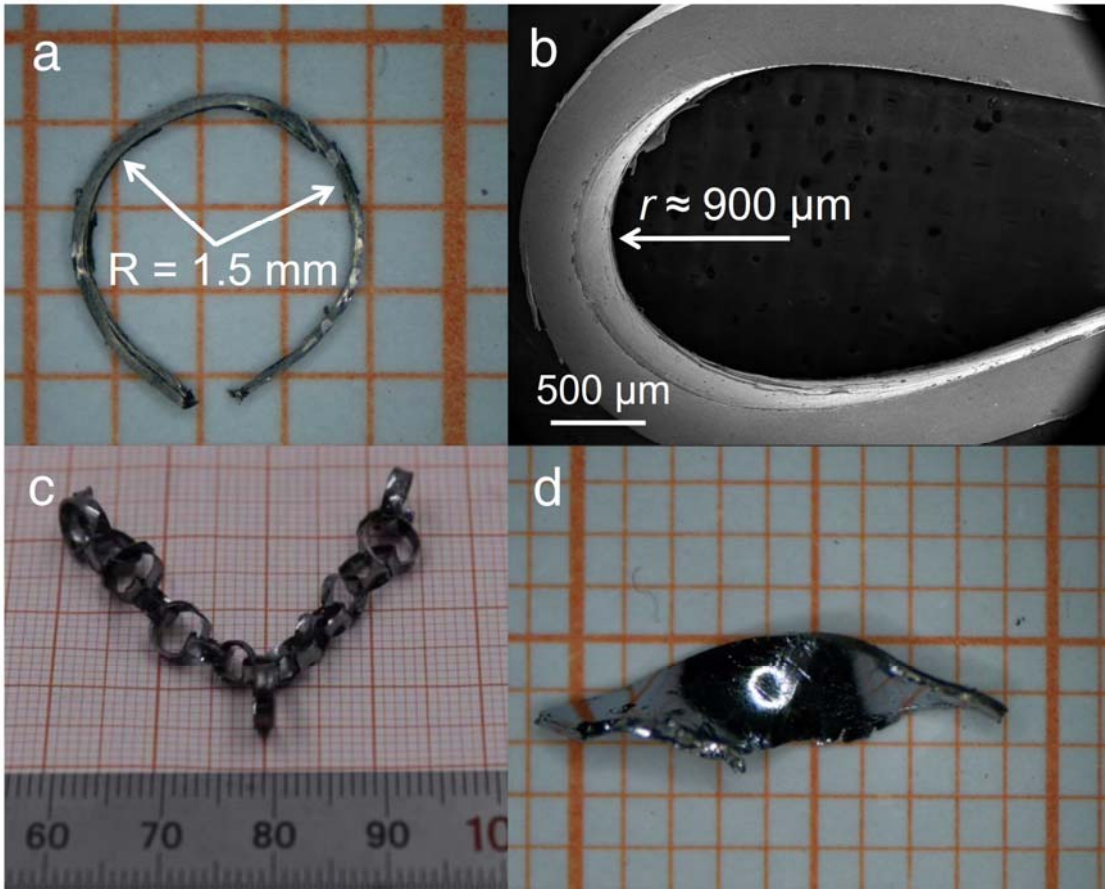

Supplementary Figure 4. Deformed α-Mg_3Bi_2 crystal slabs. a, The crystal slab with a thickness of 175 μm showed a small bending radius of 1.5 mm. **b**, The SEM image of a bent crystal slab, and the thickness is about 273 μm. **c**, A flexible chain deformed by crystal slabs. **d**, A twisted crystal slab. α-Mg_3Bi_2 crystal slabs can be morphed into various shapes without breaking.

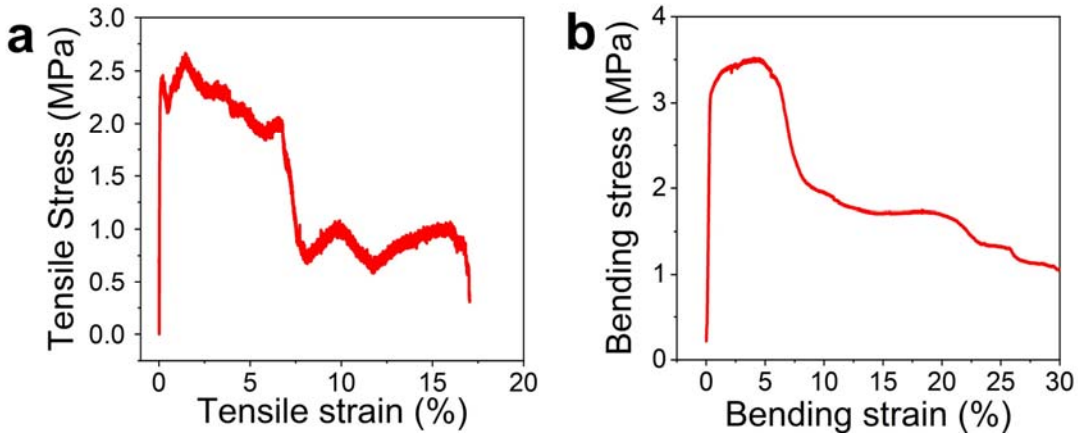

Supplementary Figure 5. Mechanical properties of α-Mg_3Bi_2. The stress-strain curves of biaxial tensile test (**a**) and three-point bending test (**b**).

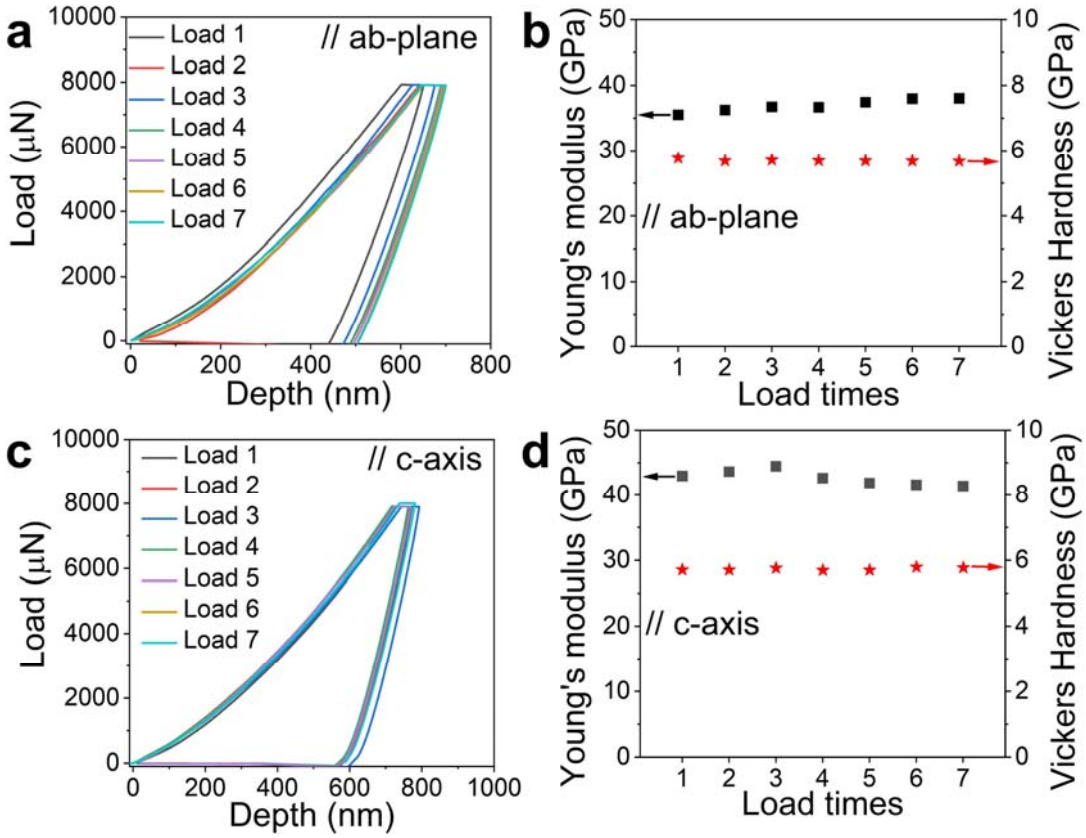

Supplementary Figure 6. The nanoindentation tests. a, The nanoindentation tests along ab-plane. **b**, Young's modulus, and Vickers Hardness along ab-plane. **c**, The nanoindentation tests along c-axis. **d**, Young's modulus, and Vickers Hardness along c-axis.

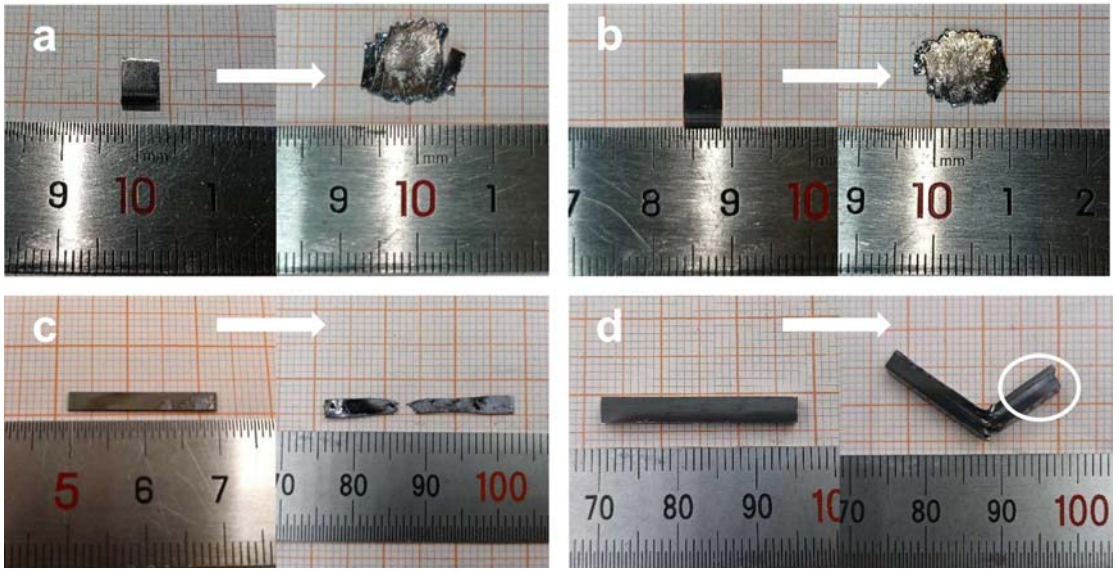

Supplementary Figure 7. Images of the sample before and after mechanical property testing. The samples for compression tests along the ab-plane (**a**) and c-axis (**b**). Samples for tensile (**c**) and three-point bending tests (**d**). These pictures show alterations in these samples before and after mechanical tests.

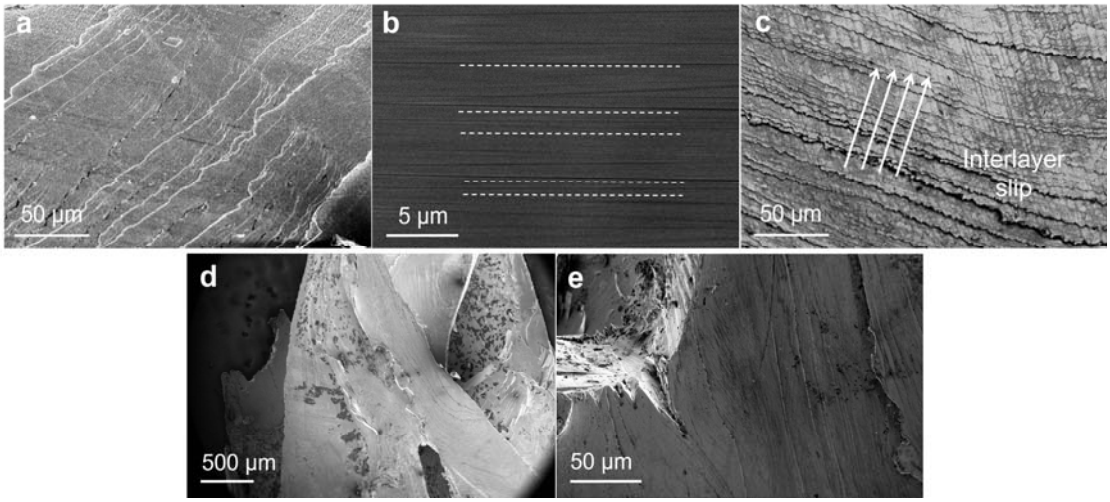

Supplementary Figure 8. SEM images of the samples before and after deformation. **a**, The fresh cleavage surface of α-Mg_3Bi_2, showing obvious layer structures. **b**, The SEM image of the sample after the compression test. There are many slip bands. **c**, After the biaxial tensile test, the cleavage plane showed many interlayer slips. (**d**, **e**) SEM images of the fractured cross section morphologies after the tension test, in which numerous interlayer slips were observed. Beyond the tensile limit, the sample underwent plastic fracture.

Supplementary Section 2: Atomic-scale locally distorted structures around helical dislocation.

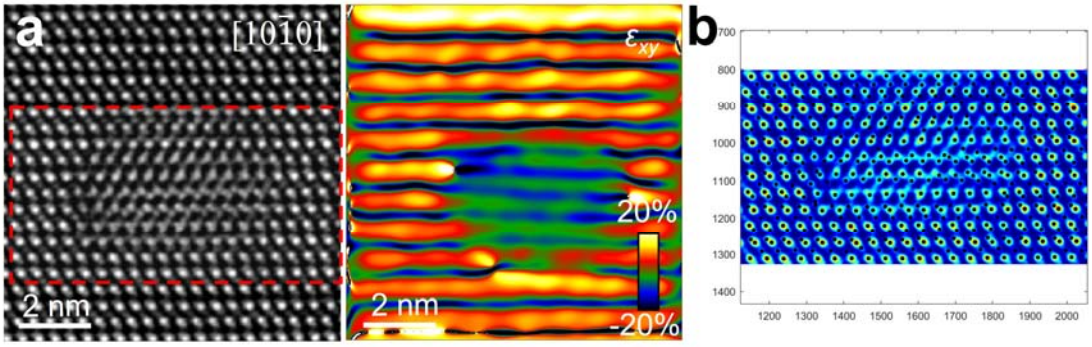

Supplementary Figure 9. HAADF-STEM images of bent p-type α-Mg_3Bi_2. a, The atomic resolution iDPC image of another area in α-Mg_3Bi_2 along the [10$\bar{1}$0] orientation and the corresponding strain map. **b**, The average ellipse and it mass center of α-Mg_3Bi_2 (marked in the red box in Supplementary Figure 9a) generated using CalAtom software.

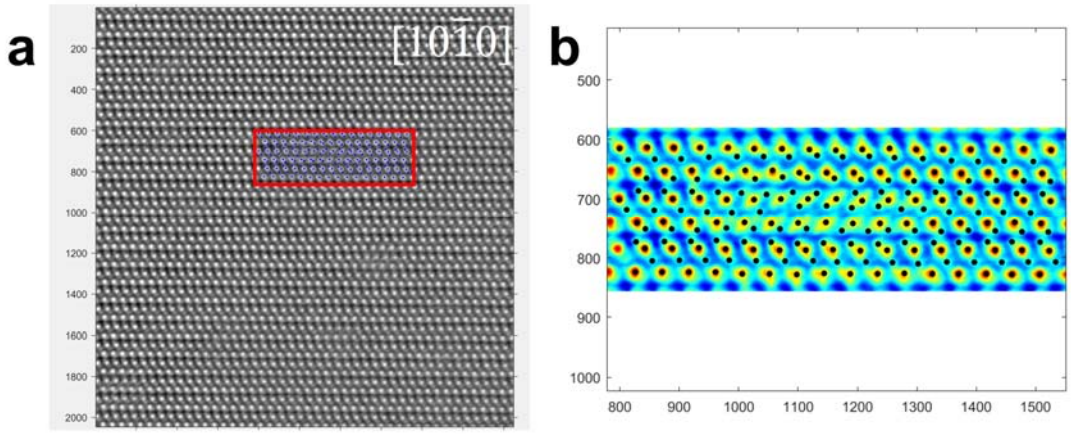

Supplementary Figure 10. Atomic-scale observations of strain-induced locally distorted structures. a, The atomic-resolution iDPC image of α-Mg_3Bi_2 along the [10$\bar{1}$0] orientation with strain. **b**, The average ellipse and its mass center of α-Mg_3Bi_2 determined using CalAtom software (marked by the red box in Supplementary Figure 10a, including 13 rows of atoms).

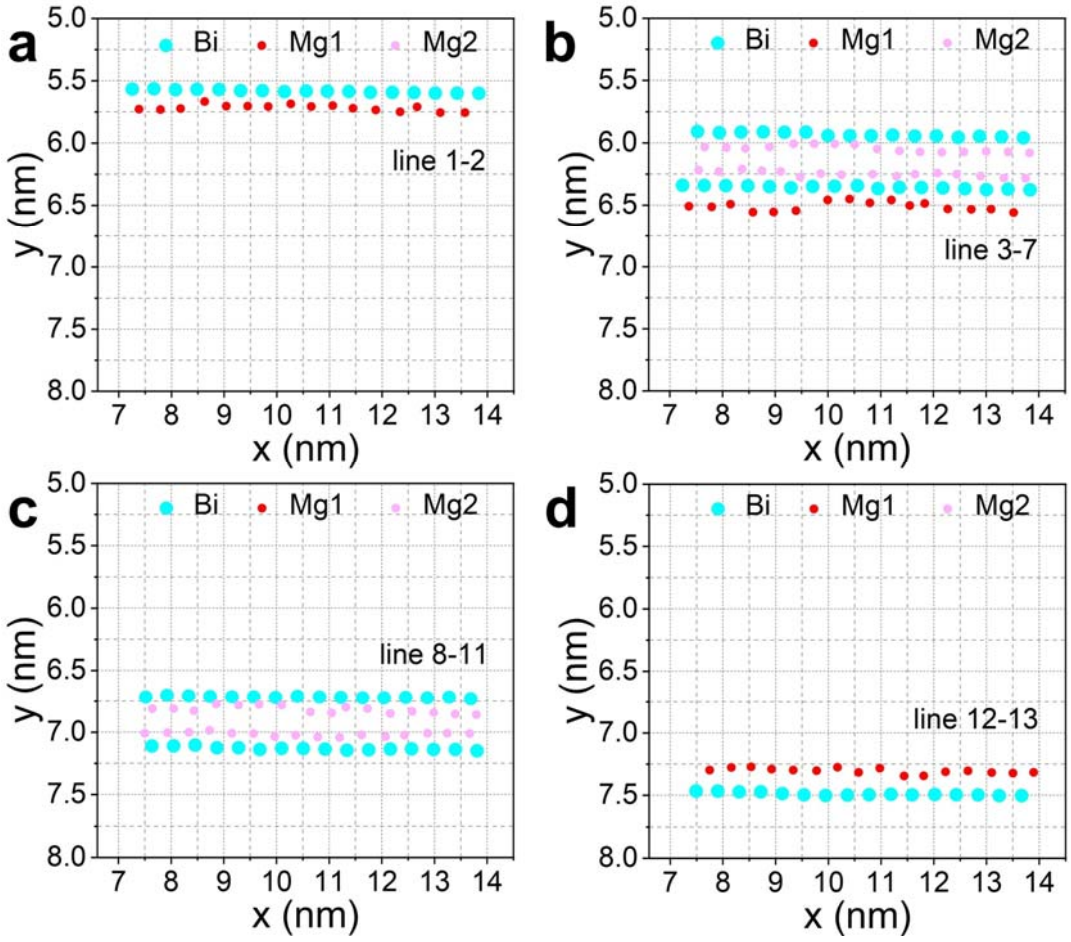

Supplementary Figure 11. Atom-column displacement maps for 13 lines of Mg and Bi atoms, generated using CalAtom software.

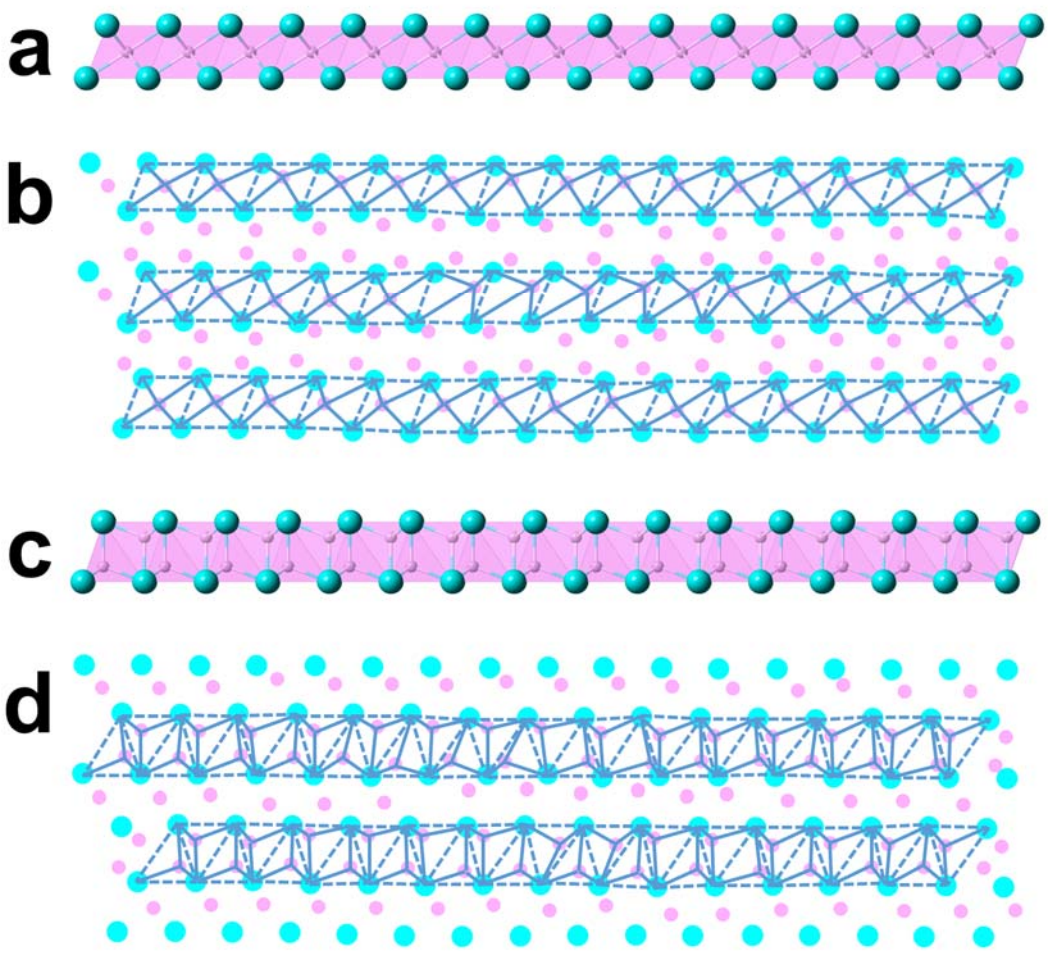

Supplementary Figure 12. Distortion of interlayer MgBi6 and intralayer MgBi4 polyhedra around helical dislocation as shown in Figs. 2e and 2g. a, The initial interlayer MgBi6 octahedra. **b**, The distorted interlayer MgBi6 octahedron. **c**, The initial intralayer MgBi4 tetrahedra. **d**, The distorted interlayer MgBi4 octahedron.

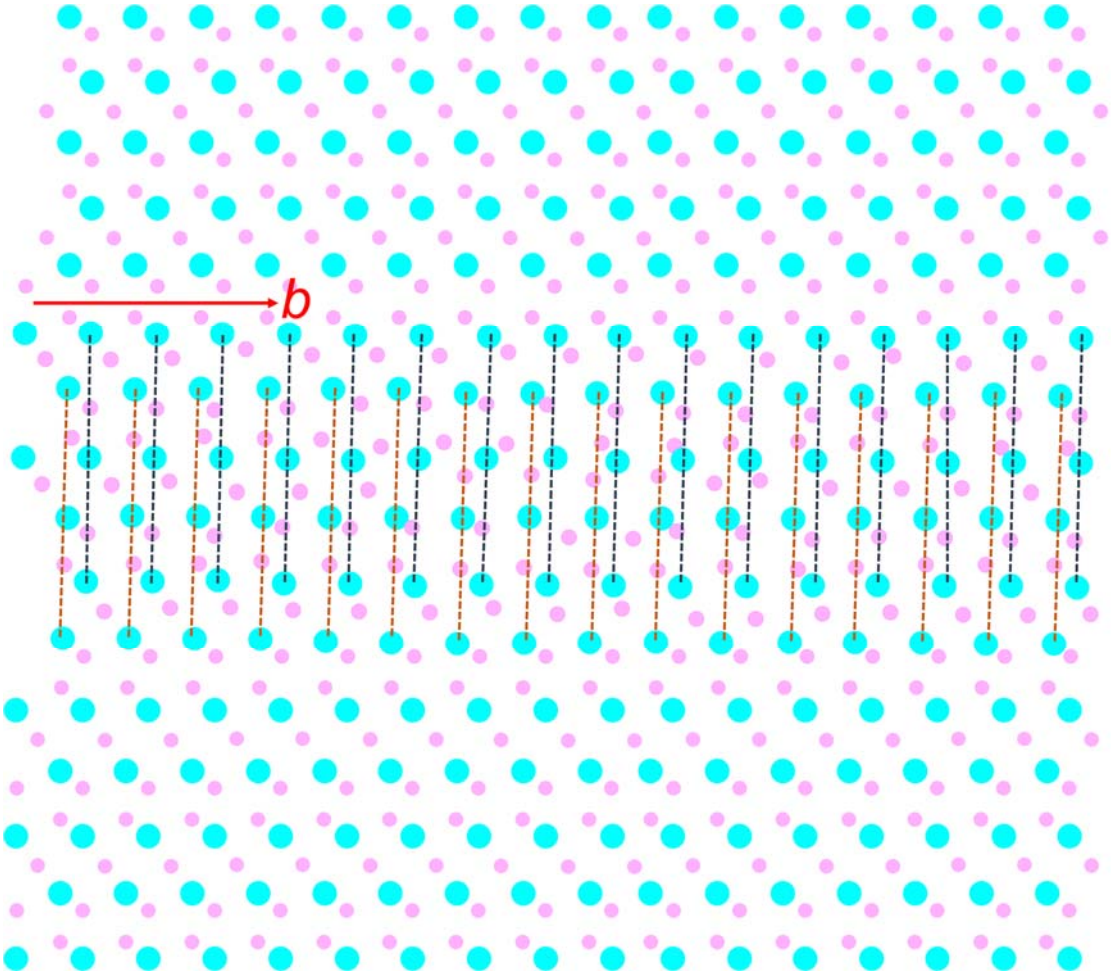

Supplementary Figure 13. The structure model of helical dislocation based on the TEM results. The solid red arrow represents the Burgers vector (*b*).

Supplementary Section 4: The crystal structure used for ab initio molecular dynamics (AIMD) simulations.

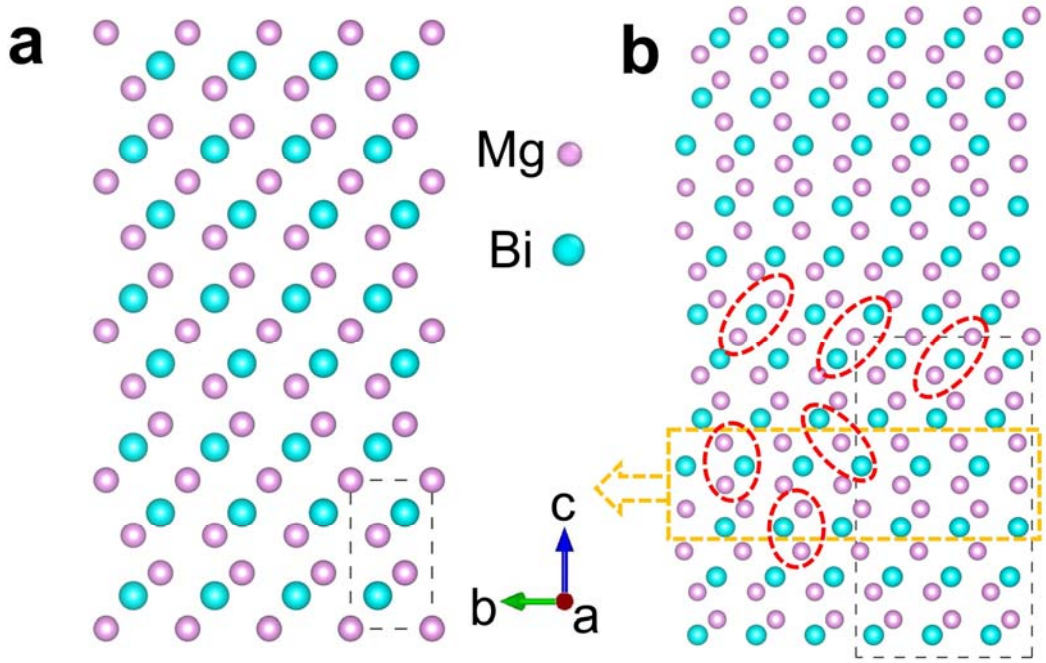

Supplementary Figure 14. The crystal structure used for ab initio molecular dynamics (AIMD) simulations. a, The structure of α-Mg_3Bi_2 viewed along the [10$\bar{1}$0]. **b**, The optimized supercell of α-Mg_3Bi_2 with layer slip by half a cycle (the slip direction is indicated by yellow arrow). The supercell of α-Mg_3Bi_2, containing 135 atoms, was optimized with layer slip distortion. As shown in Supplementary Fig. 14b, the optimized supercell with distortion forms a specific helical dislocation, which results in a unique reorientation or flipping of the atomic arrangement around the dislocation planes, highlighted in the red circle.

Supplementary Section 5: Chemical bonding analysis α-Mg_3Bi_2 by DFT calculation

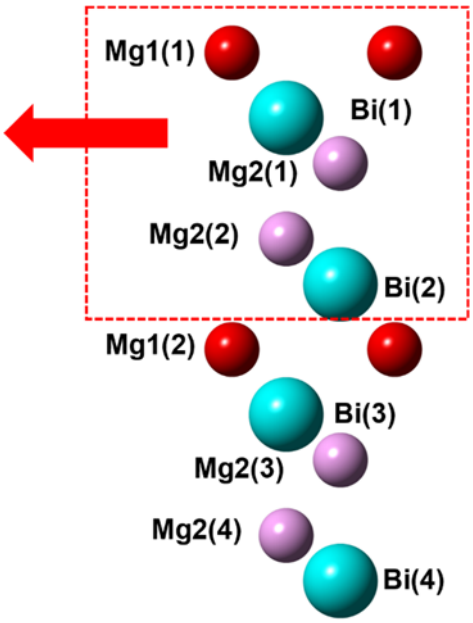

Supplementary Figure 15. The schematic diagram of the (0001)[01$\bar{1}$0] slip system.

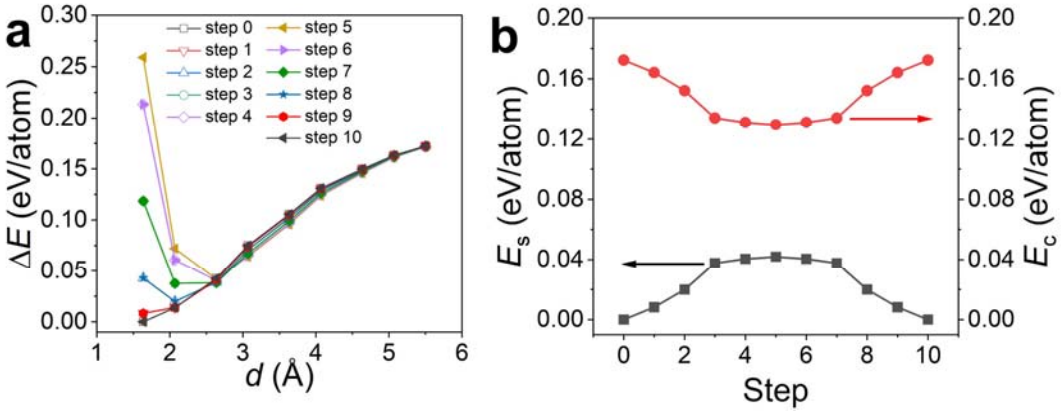

Supplementary Figure 16. Plastic properties of *α*-Mg_3Bi_2. a, Energy variation as a function of the interlayer distance (*d*) for each step through slipping. **b**, The step-by-step variations of slipping energy E_s and cleavage energy E_c through slipping.

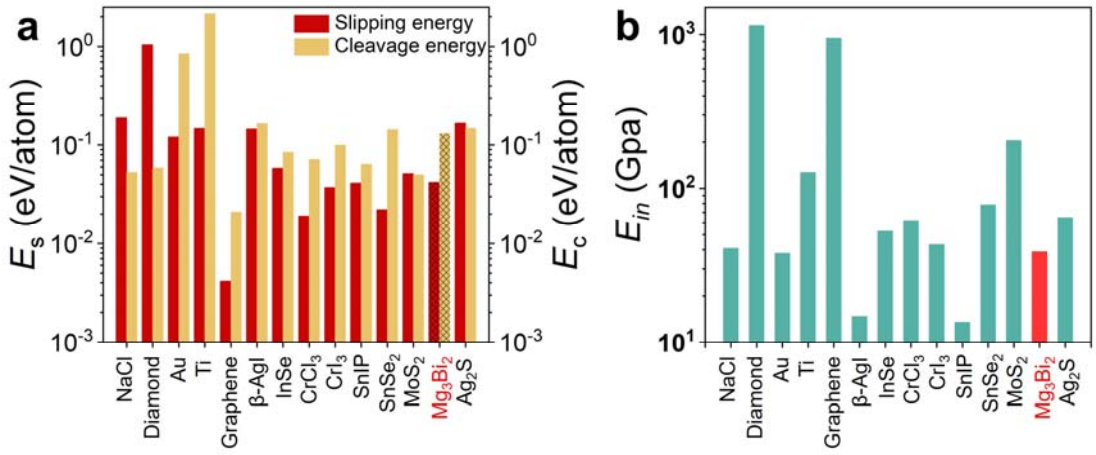

Supplementary Figure 17. Plastic properties of α-Mg_3Bi_2 along with other typical materials. **a**, calculated slipping energy (E_s), cleavage energy (E_c); **b**, intralayer Young's modulus E_{in} of α-Mg_3Bi_2 and several other materials, and details are listed in Supplementary Table 1[30,32,34,35].

Supplementary Section 5: Thermoelectric performances of n-type and p-type α-Mg_3Bi_2 crystals

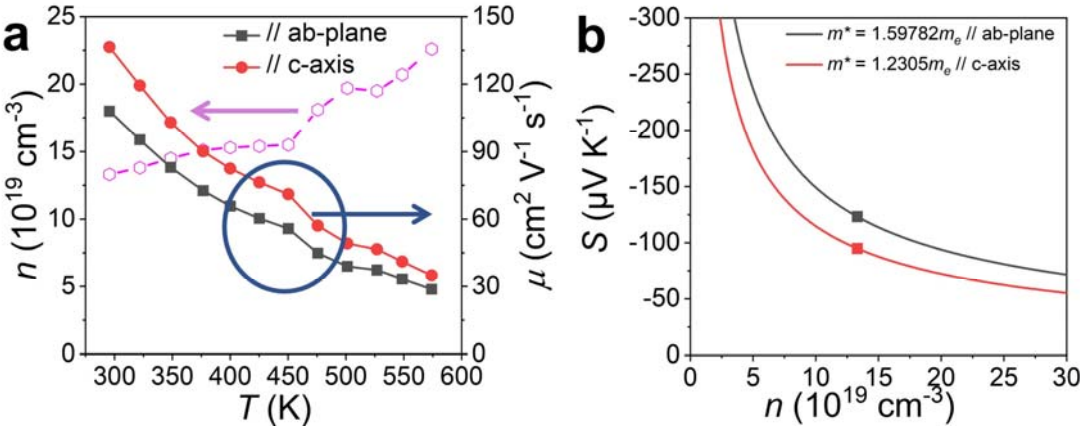

Supplementary Figure 18. Transport properties for n-type α-Mg_3Bi_2 crystals. a, Temperature-dependent carrier concentration (n) and Hall mobility (μ) of n-type α-Mg_3Bi_2 crystal. **b**, Experimental data versus calculated plots of Seebeck coefficient. The solid line connecting the scatter was predicted from a single parabolic band model, and m^* is the density of states effective mass.

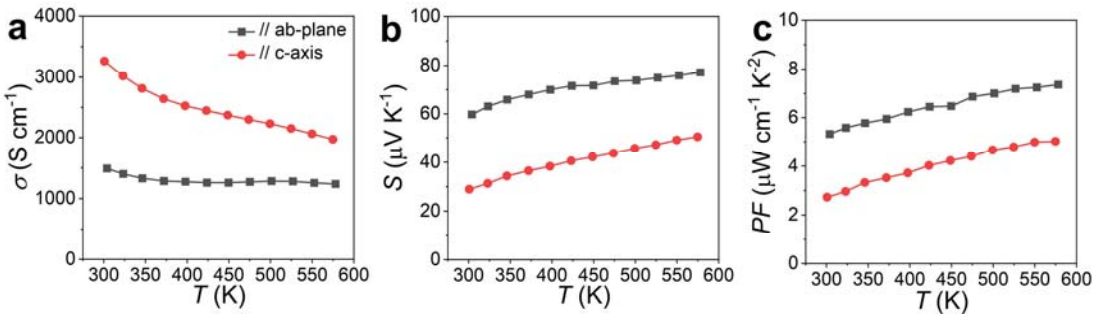

Supplementary Figure 19. Transport properties for p-type α-Mg_3Bi_2 crystals. Temperature-dependent electrical conductivity (**a**), Seebeck coefficient (**b**), and power factor (**c**) of p-type α-Mg_3Bi_2 crystal.

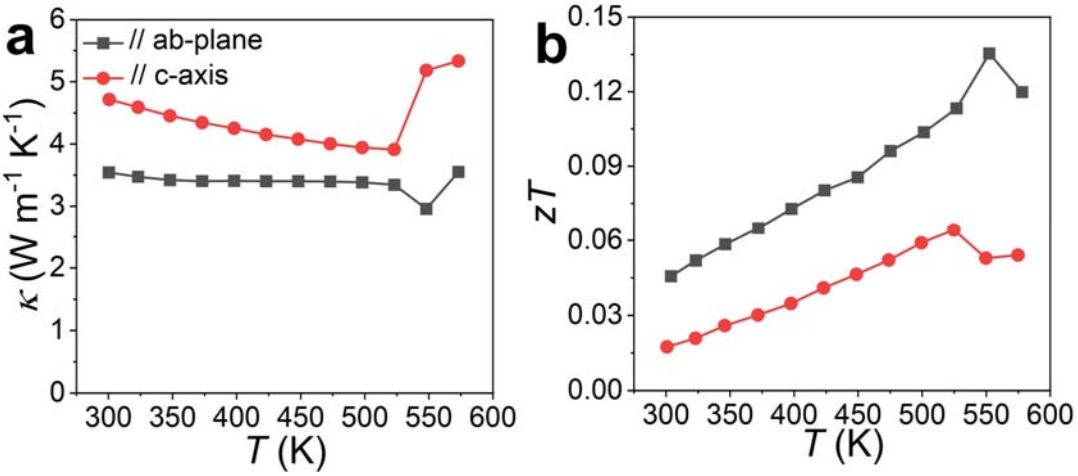

Supplementary Figure 20. Transport properties for p-type α-Mg_3Bi_2 crystals. Temperature-dependent thermal conductivity (**a**) and *zT* value (**b**) of p-type α-Mg_3Bi_2 crystal.

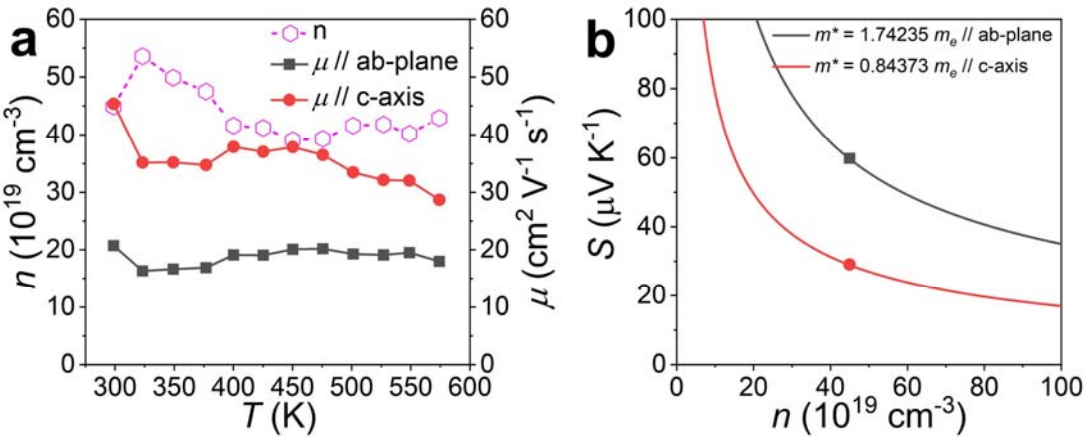

Supplementary Figure 21. Transport properties for p-type *α*-Mg_3Bi_2 crystals. a, Temperature-dependent carrier concentration (n) and Hall mobility (μ) of p-type α-Mg_3Bi_2 crystal. **b**, Experimental data versus calculated plots of Seebeck coefficient. The solid line connecting the scatter was predicted from a single parabolic band model.

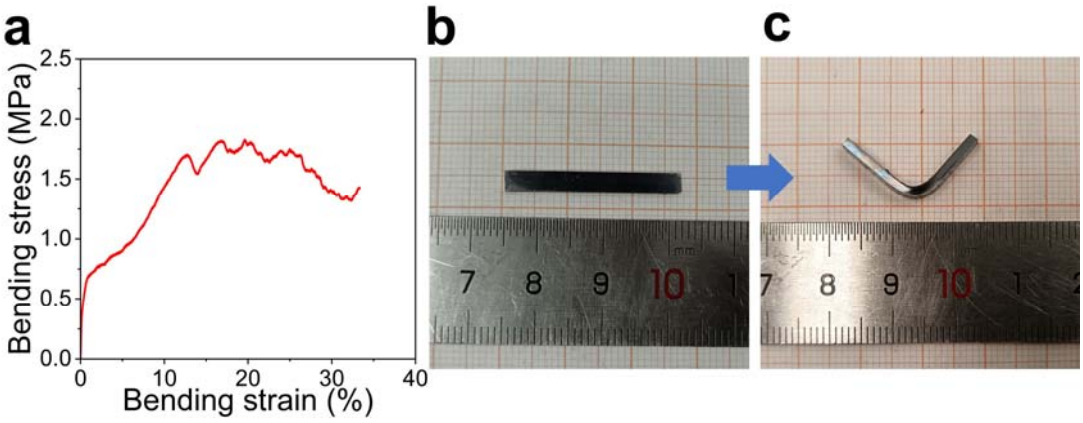

Supplementary Figure 22. Mechanical properties of n-type Te-doped *α*-Mg_3Bi_2. a, The stress-strain curve of three-point bending test. **b**, Single-crystal specimens used for three-point bending tests (3.07×1.52×6.46 mm^3). **c**, The bent sample of n-type *α*-Mg_3Bi_2 crystal. The n-type *α*-Mg_3Bi_2 crystals also exhibited >30% bending strain.

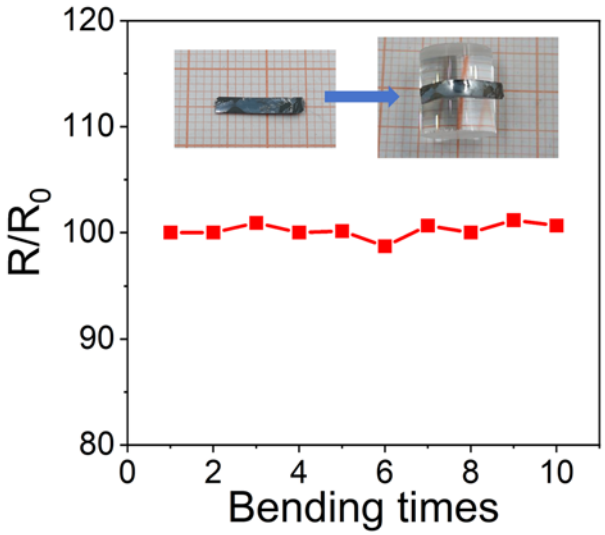

Supplementary Figure 23. Variations of electrical resistance with deformation cycles. The thickness of the α-Mg_3Bi_2 crystal slab is about 477 μm, and the bending radius is 4.5 mm.

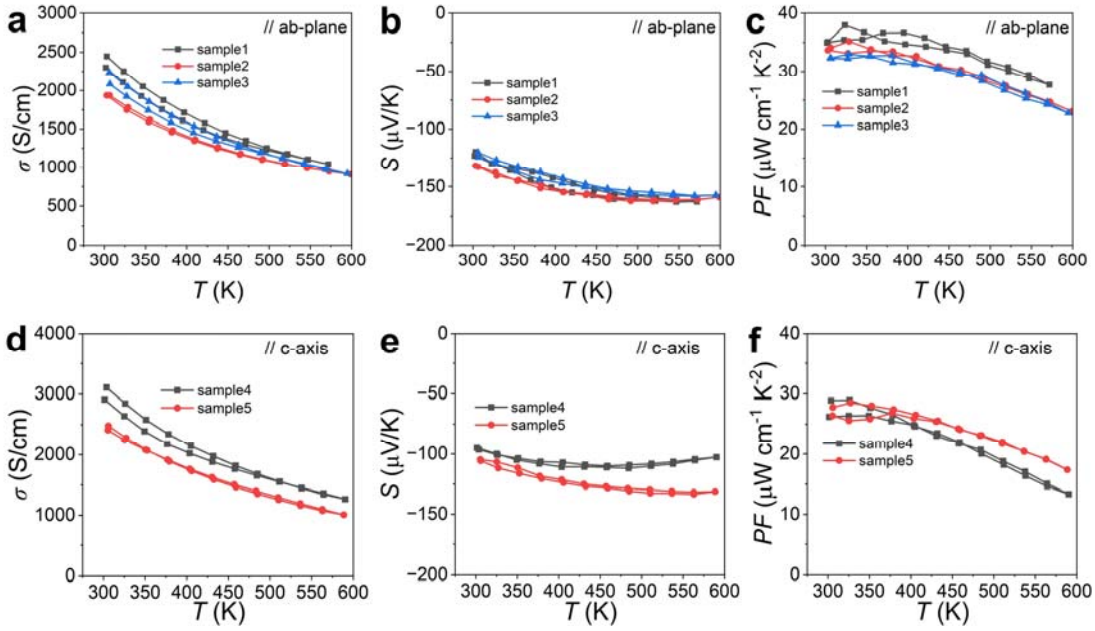

Supplementary Figure 24. Repeat tests of the thermoelectric properties of the n-type α-Mg_3Bi_2. Temperature-dependent electrical resistivity (**a**, **d**), Seebeck coefficient (**b**, **e**), and power factor (**c**, **f**). The transport properties are highly comparable among these samples, indicating the good reproducibility of the thermoelectric properties.

Supplementary Section 6: Phase, thermoelectric and mechanical performances of p-type AgCu(Se, S, Te) pseudoternary solid solutions

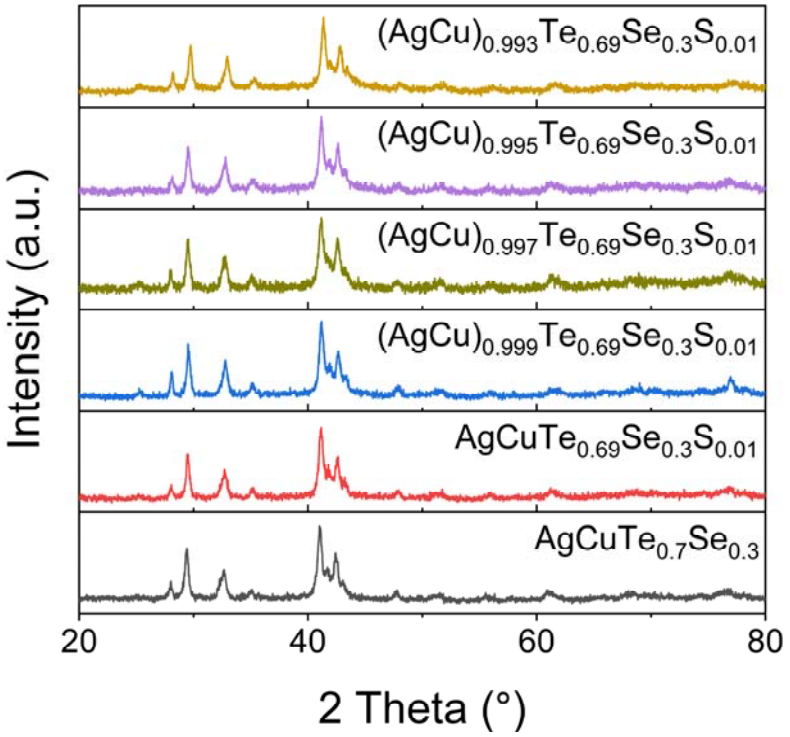

Supplementary Figure 25. The power XRD patterns of p-type AgCu(Se, S, Te) pseudoternary solid solutions in this job, which matched with that for Yang' work[6].

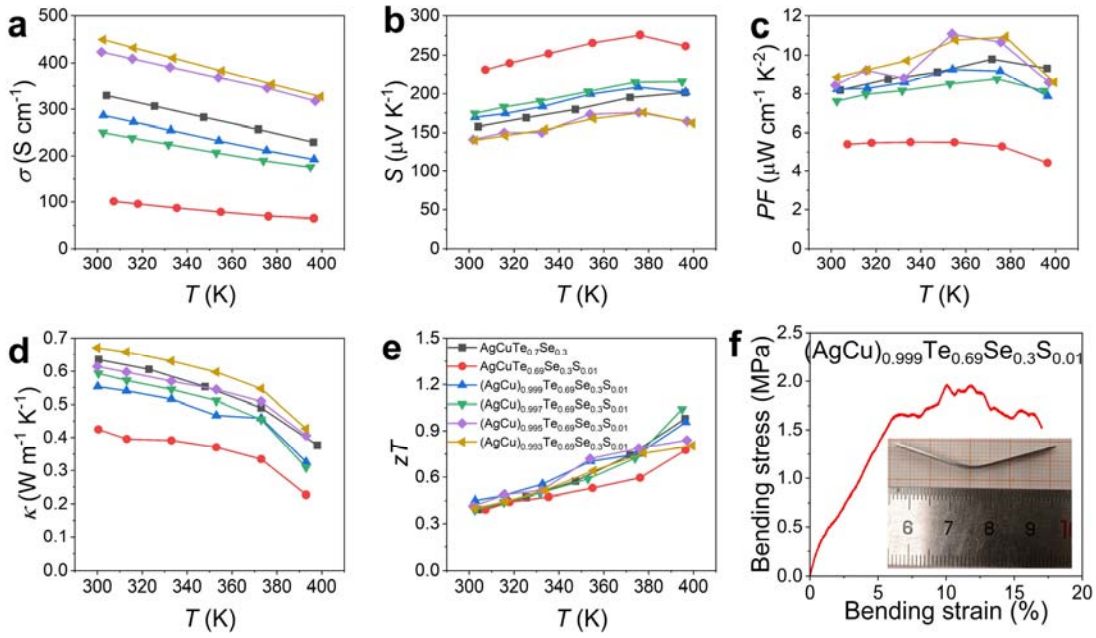

Supplementary Figure 26. Thermoelectric and mechanical performances of p-type AgCu(Se, S, Te) pseudoternary solid solutions. (**a-e**) Temperature-dependent electric and thermal transport properties of p-type $AgCuTe_{0.7}Se_{0.3}$-based ingots. In the $(AgCu)_{0.999}Te_{0.69}Se_{0.3}S_{0.01}$ ingot, we obtained best thermoelectric performance with room-temperature *zT* value of 0.45, max *zT* value of 0.96 at 393 K, and the average *zT* value was 0.66 between 300-400 K. **f**, The stress-strain curves of three-point bending test for $(AgCu)_{0.999}Te_{0.69}Se_{0.3}S_{0.01}$ slab (4.43*0.58*40.15 mm^3), which exhibited a bending strain greater than 17%.

Supplementary Section 7: The Module fabrication of f-TEGs and output performances

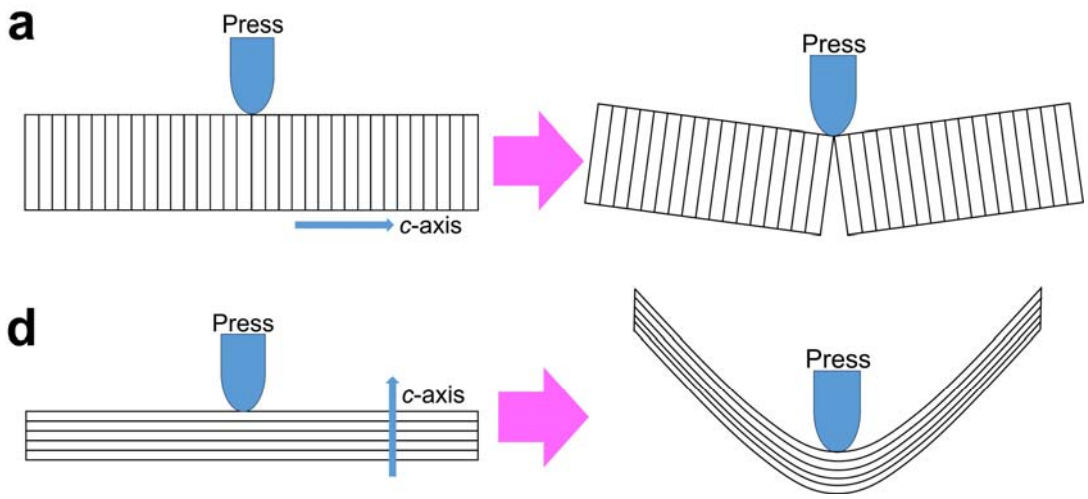

Supplementary Figure 27. Fracture models under stress in different crystallographic directions (**a**. Press along ab-plane; **b**. press in c-axis) for α-Mg_3Bi_2 crystal. The interlayer Mg1-Bi chemical bonds are relatively weak, and α-Mg_3Bi_2 easily dissociates along the ab-plane. When subjected to stress along the ab-plane, the samples are prone to dissociation, leading to an open circuit in the device. Although the thermoelectric performance along the c-axis is not optimal, it is suitable for the out-of-plane devices.

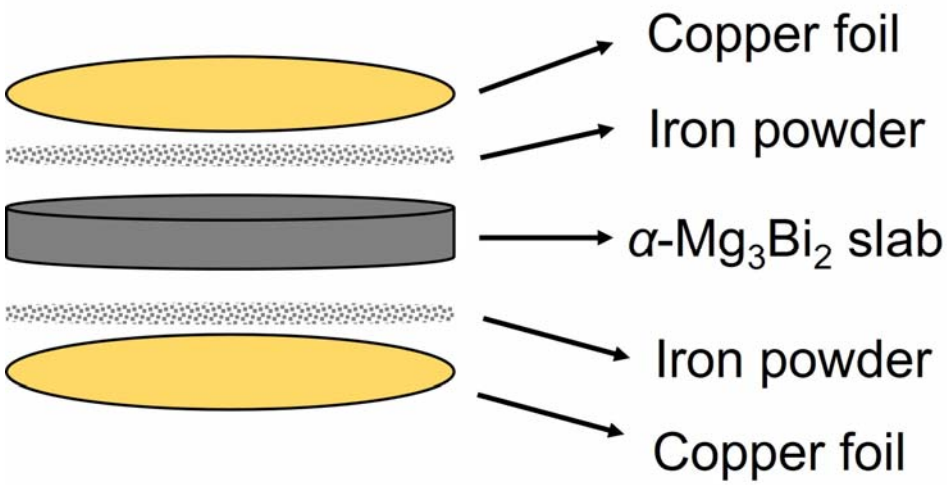

Supplementary Figure 28. Schematic of the preparation of Cu/Fe/α-Mg_3Bi_2/Fe/Cu layer structure.

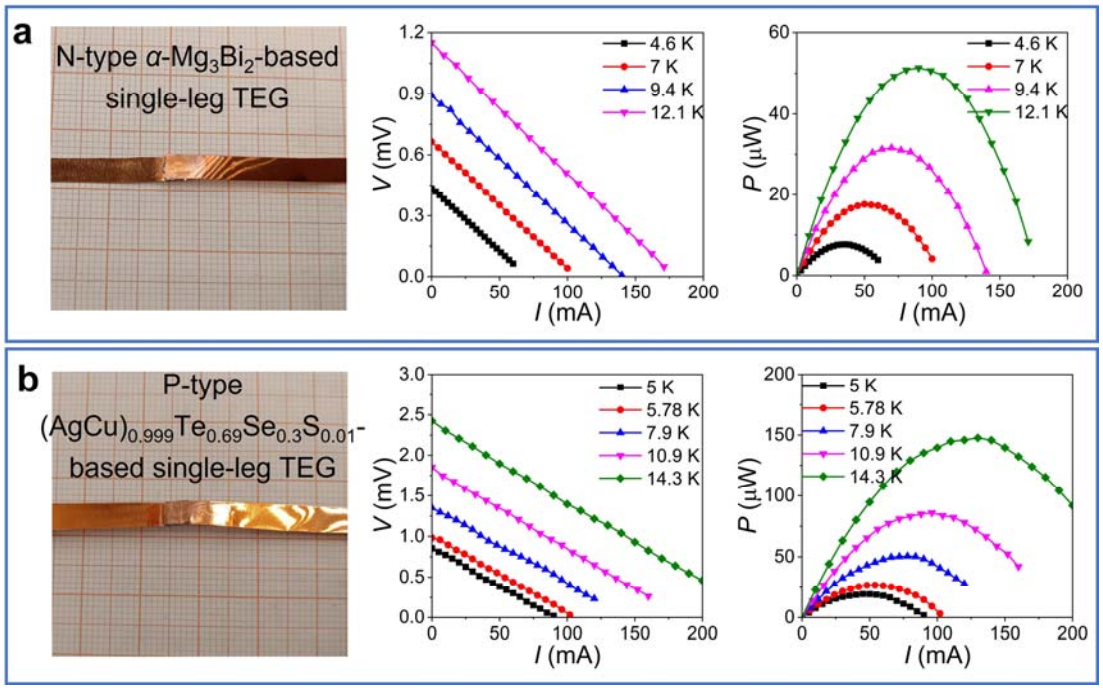

Supplementary Figure 29. Output performances of n-type and p-type single-lag TEGs. a, The n-type α-Mg_3Bi_2-based single-leg TEG, and its output performance. **b**, p-type $(AgCu)_{0.999}Te_{0.69}Se_{0.3}S_{0.01}$-based single-leg TEG, and its output performance.

The as-prepared n-type α-Mg_3Bi_2 crystal and p-type $(AgCu)_{0.999}Te_{0.69}Se_{0.3}S_{0.01}$ ingots were cut into thin plates with the thickness about 330 μm by using the diamond wire cutting. The metallic barrier layers were both prepared for n-type and p-type materials by using spark plasma sintering (SPS- 211LX) at 773 K under a pressure of 50 MPa for 5 min, as shown in Supplementary Fig. 28. Then the plates were cut into square thermoelectric legs of 4 × 4 mm^2 by using the diamond wire cutting. The single-leg TEGs were fabricated by placing n-type and p-type legs between copper foils, as shown in Supplementary Figs. 29a and 29b. For n-type single-leg TEG, the measured open circuit voltage (V_{oc}) and maximum output power (P_{max}) were 1.151 mV and 51.4 μW, respectively, under a temperature gradient (ΔT) of 12.1 K. For p-type single-leg TEG, the measured open circuit voltage (V_{oc}) and maximum output power (P_{max}) were 2.43 mV and 147.7 μW, respectively, under a temperature gradient (ΔT) of 14.3 K. In a word, the output performance of the six-couple out-of-plane f-TEG, as shown in Fig. 5, benefits from the combined contributions of the n-type and p-type legs.

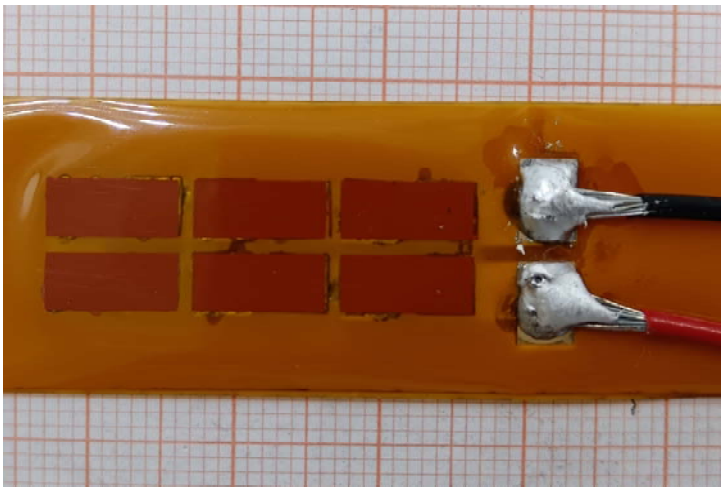

Supplementary Figure 30. Optical images of the as-prepared six-couple flexible TE devices with filling factors of 73.5%. And the thickness of this flexible TE was only 0.88 mm.

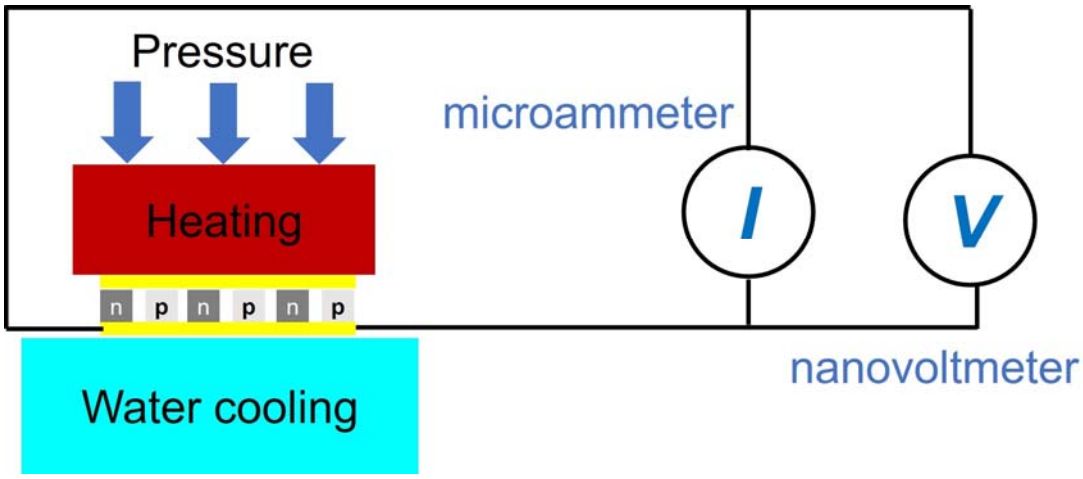

Supplementary Figure 31. Homemade apparatus for testing the output performance of f-TEG.

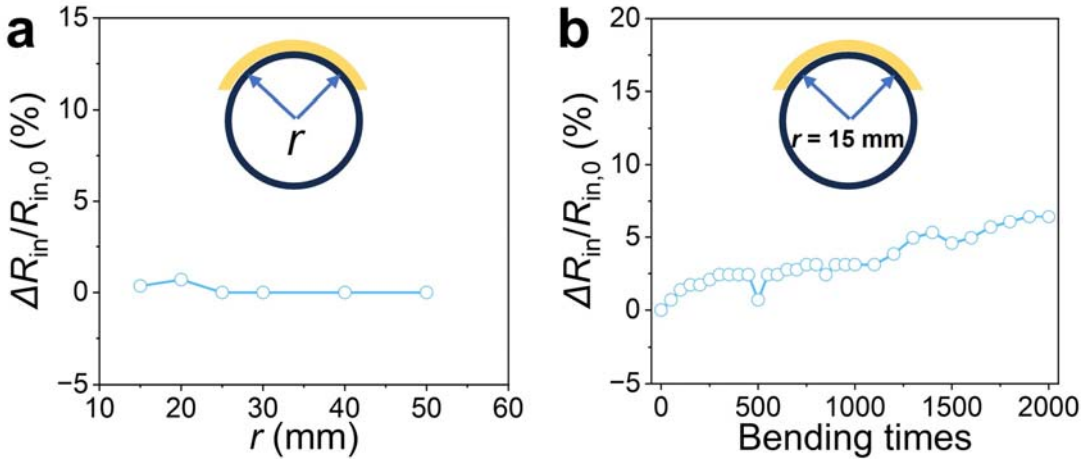

Supplementary Figure 32. Service stability of the f-TEG devices. a, $\Delta R_{in}/R_{in,0}$ of the 6-couple flexible devices with different bending radius. **b**, $\Delta R_{in}/R_{in,0}$ of the 6-couple flexible devices in the bending test with the bending radius of 15 mm.

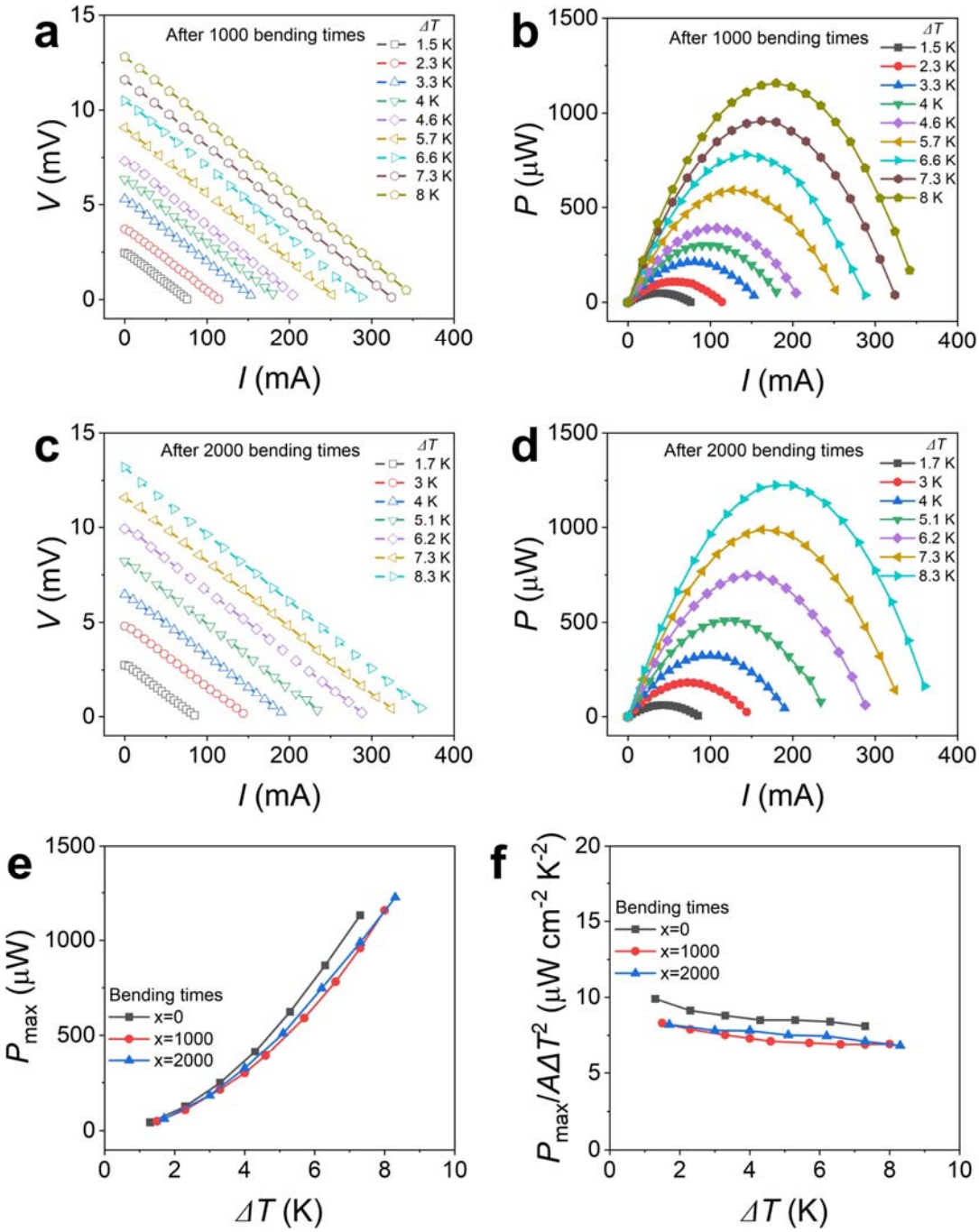

Supplementary Figure 33. Service stability of the f-TEG devices. (**a**, **b**) The output performance of the device after 1000 bending times. Current (I) dependencies of the output voltage (V) and output power (P). (**c**, **d**) The output performance of the device after 2000 bending times. **e**, Bending time-dependent maximum output power (P_{max}). **f**, Bending time-dependent maximum normalized power density ($P_{max}/A\Delta T^2$).

Supplementary Table 1.

Plastic properties of α-Mg_3Bi_2 along with other typical materials. Band gap, space group, calculated slipping energy E_s, cleavage energy E_c, in-plane modulus E_{in} along the slipping direction, and the deformability factor Ξ of selected materials[30,32,34,35].

Materials	Bandgap (eV)	Space group	E_s (eV/atom)	E_c (eV/atom)	E_{in} (Gpa)	Slip & cleavage system	Ξ factor (Gpa^{-1})	Ref.
NaCl	8.7	$Fm\bar{3}m$	0.188	0.0527	41	(001) [100]	0.0068	30
Diamond	5.6	$Fd\bar{3}m$	1.041	0.0585	1149	(111) [1-10]	0.000049	30
Au	0	$Fm\bar{3}m$	0.12	0.85	38	(110) [1-10]	0.19	30
Ti	0	$P6_3/mmc$	0.147	2.149	128	(001) [100]	0.11	30
Graphere	0	$P6_3/mmc$	0.00413	0.0209	951	(001) [100]	0.0053	30
β-AgI	3	$P6_3mc$	0.145	0.165	14.8	(001) [100]	0.077	30
InSe	1.2	$P6_3/mmc$	0.058	0.0844	53	(001) [100]	0.027	30
$CrCl_3$	1.53	C2/m	0.019	0.0716	62.1	(001) [010]	0.06104	32
CrI_3	1.58	C2/m	0.037	0.0997	43.4	(001) [010]	0.0633	32
SnIP	1.8	P12/c1	0.041	0.064	13.6	[100]	0.1148	34
$SnSe_2$	1	$P\bar{3}m1$	0.022	0.143	78.77	(001)[120]	0.0821	35
MoS_2	1.491	$P6_3/mmc$	0.0511	0.0499	206	(001) [100]	0.0047	30
α-Mg_3Bi_2	0	$P\bar{3}m1$	0.04184	0.13051	39	(0001) [0100]	0.08	This work
Ag_2S	1.01	P21/c	0.166	0.148	65	(100) [001]	0.014	30

Supplementary Table 2.

Thermoelectric performances of α-Mg_3Bi_2 along with other typical materials. The electrical conductivity (σ), Seebeck coefficient (S), and power factor (PF) of some inorganic plastic thermoelectric semiconductors[6,20-29,31,39].

Materials	σ (S cm^{-1})	S (μV K^{-1})	PF (μW cm^{-1} K^{-2})	Ref.
α-Mg_3Bi_2 // ab-plane	2230	-123.3	35	This
α-Mg_3Bi_2 // c-axis	2907.4	-95	26.2	work
$(AgCu)_{0.998}Se_{0.22}S_{0.08}Te_{0.7}$	83.4	246.6	5.1	6
$Ag_2Se_{0.69}S_{0.31}$	1324	-120	22	20
$Ag_{3.96}SSe$	345.4	-121.5	5.26	21
$Ag_2S_{0.5}Se_{0.45}Te_{0.05}$	270	-136	4.496	22
$Ag_2S_{0.8}Te_{0.2}$	390	-101	3.98	22
$Ag_2S_{0.5}Se_{0.5}$	300	-123	4.84	22
$Ag_2Se_{0.6}S_{0.4}$	600	-100	6	23
$Ag_2Te_{0.7}S_{0.3}$	1050	-65	4.44	24
$Ag_{3.95}TeS$	130	-195	5.16	25
$Ag_{20}S_{7.1}Te_{2.9}$	275.3	-128	4.5	26
$Ag_2S_{0.6}Te_{0.4}$ fiber	420	-115	6.63	27
$Ag_2S_{0.45}Se_{0.45}Te_{0.1}$	659.6	-91	5.8	28
$Ag_2S_{1/3}Se_{1/3}Te_{1/3}$	600	-100	6	29
$Cu_{0.005}SnSe_{1.95}Cl_{0.05}$ (375K)	268	-259.4	18	31
$Cu_{0.005}SnSe_{1.95}Br_{0.05}$ (375 K)	390	-218.6	18.5	
$Mg_{3.2}Bi_{1.998}Te_{0.002}$ // *ab*-plane	1429	-200	55	39
$Mg_{3.2}Bi_{1.998}Te_{0.002}$ // *c*-plane	2356	-57	7.65	

Supplementary Table 3.

Output performances of flexible thermoelectric devices.

Flexible devices	ΔT (K)	$P_{max}/A\Delta T^2$	Ref.
n-$Mg_{3.2}Bi_{1.498}Sb_{0.5}Te_{0.002}$ + p-$Bi_{0.4}Sb_{1.6}Te_3$	10	5.7	41
	20	5.5	
	30	5.5	
	40	5.4	
	50	5.5	
n-$Mg_{3.2}Bi_{1.498}Sb_{0.5}Te_{0.002}$ + Cu wire	7.2	2.04E-5	40
	13.1	2.08E-5	
p-$(AgCu)_{0.998}Se_{0.22}S_{0.08}Te_{0.7}$ + n-$Ag_{20}S_3Te_7$	2.2	30	6
Ag_2Se network-based device	16	15.6E-3	42
Bi_2Te_3 + Sb_2Te_3 on Si	20	0.3475	43
Bi_2Te_3 + Sb_2Te_3 on glass fabric	47.5	1.58	44
Screen-printed $Bi_{0.5}Sb_{1.5}Te_3$ + $Bi_2Te_{2.7}Se_{0.3}$	25	7.6	45
Bi_2Te_3-based	50	6.68E-4	46
Bi_2Te_3-based	150	8.22	47
PEDOT-based	10	2.33E-4	9
poly(metal 1,1,2,2-ethenetetrathiolate)-based	30	1.31E-3	48
Carbon nanotube yarn-based	48	2.32E-3	49
PEDOT:PSS (p) + fullerene derivative (n)	25	4.86E-5	50

Supplementary Table 4.

Room temperature mechanical properties of α-Mg_3Bi_2.

Compression		**Tension**			**Bending**			**Vickers Hardness**	**Young's modulus**
Modulus (GPa)	Yield strength (MPa)	Modulus (GPa)	Yield strength (MPa)	Fracture strength (MPa)	Modulus (GPa)	Yield strength (MPa)	Fracture strength (MPa)	(GPa)	(GPa)
0.51 (// *ab*-plane)	17.43 (// *ab*-plane)	5.405	2.462	2	1.044	3.38	-	5.7 (// *ab*-plane)	36.95 (// *ab*-plane)
5.69 (// *c-axis*)	116.44 (// *c-axis*)							5.72 (// *ab*-plane)	42.79 (// *c-axis*)

Supplementary Table 5.

Partial refined results from neutron diffraction data of small-sized α-Mg_3Bi_2 single crystals before and after bending at room temperature.

Partial refined results of Mg_3Bi_2 single crystals before bending					
Peak Index	Peak type	Area Integral	FWHM (Å)	Max Height	Center Peak (Å)
Mg2-Bi	Gaussian	0.09078	0.14063	0.60645	2.81752
Mg2-Bi	Gaussian	0.38102	0.18803	1.90366	2.91462
Mg1-Bi	Gaussian	0.43247	0.24994	1.62549	3.0348
Mg2-Mg2	Gaussian	0.41614	0.39024	1.00184	3.23349
Mg1-Mg2	Gaussian	0.16379	0.3851	0.39957	3.71541
Bi-Bi	Gaussian	0.27019	0.42879	0.59223	4.5412
Mg1-Mg1	Gaussian	0.87816	0.33706	2.45185	4.72673
Partial refined results of Mg_3Bi_2 single crystals after bending					
Peak Index	Peak type	Area Integral	FWHM (Å)	Max Height	Center Peak (Å)
Mg2-Bi	Gaussian	0.8122	0.17459	0.43843	2.77755
Mg2-Bi	Gaussian	0.58836	0.2338	2.3653	2.90201
Mg1-Bi	Gaussian	0.62382	0.29129	2.01193	3.06633
Mg2-Mg2	Gaussian	0.22421	0.28499	0.73907	3.30314
Mg1-Mg2	Gaussian	0.51032	0.82473	0.58183	3.66774
Bi-Bi	Gaussian	0.44629	0.50414	0.83213	4.45084
Mg1-Mg1	Gaussian	1.00426	0.36757	2.57516	4.72062

Supplementary Table 6.

The values of integrated crystal orbital Hamilton population of different Mg-Bi bonds, as shown in Figs. 3d-3f, for steps 0-5 during slip along the [01$\bar{1}$0] direction.

Bonds	**-ICOHP (eV)**		
Step	**Step 0**	**Step 2**	**Step5**
Mg1(2)-Bi(2)	0.1944	0.334	0.399
Mg1(2)-Bi(3)	0.245	0.224	0.205
Mg2(2)-Bi(1)	0.408	0.385	0.373
Mg2(2)-Bi(2)	0.333	0.383	0.339
Mg2(4)-Bi(3)	0.231	0.259	0.283
Mg2(3)-Bi(3)	0.252	0.249	0.234

Supplementary Table 7.

Thermoelectric performances of n-type α-Mg_3Bi_2-based materials. Electric conductivity (σ), Seebeck coefficient (S), power factor (PF), carrier concentration (n), Hall mobility (μ), effective mass (m^*), weighted mobility ($\mu_w = \mu(m^*/m_e)^{3/2}$) of some n-type α-Mg_3Bi_2-based single crystals and polycrystalline samples[30,59-66].

Materials	σ (S cm^{-1})	S (μV K^{-1})	PF (μW cm^{-1} K^{-2})	n (10^{19} cm^{-3})	μ (cm^2 V^{-1} s^{-1})	m^*/m_e	$\mu(m^*/m_e)^{3/2}$ (cm^2 V^{-1} s^{-1})	Ref.
n-Mg_3Bi_2 // *ab*-plane	2300	-123.3	35	13.3	108	1.60	218	This
n-Mg_3Bi_2 // *c*-axis	2907.4	-95	26.2	13.3	136.4	1.23	186.24	work
$Mg_{3.2}Bi_{1.998}Te_{0.002}$ // *ab*-plane	1429	-200	55	3.7	232	1.3	343.88	39
$Mg_{3.2}Bi_{1.998}Te_{0.002}$ // *c*-plane	2356	-57	7.65	3.7	397	0.89	333.33	
$Mg_{3.2}Bi_{1.998}Te_{0.002}$	1234.6	-129	20	3.25	200	0.53	77.17	59
$Mg_3Bi_{1.49}Sb_{0.5}Te_{0.01}$ // *ab*-plane	1606.9	-150	36.16	4	266	0.87	216.93	60
$Mg_3Bi_{1.49}Sb_{0.5}Te_{0.01}$ // *c*-axis	1141.7	-143	26.6	4	189	0.83	143.47	
Y:$Mg_3Bi_{1.25}Sb_{0.75}$	886.3	-214.9	40.9	4	140	1.25	195.92	61
Te:Mg_3Sb_2	531.5	-204.4	22.2	3.27	236	1.04	250.62	62
$Mg_{3.032}Y_{0.018}BiSb$	1282	-141	25.5	7.1	120	1.4	198.78	63
$Mg_3Sb_{0.6}Bi_{1.4}$	1361.7	-142.6	27.69	5.71	149	1.27	212.49	64
$Mg_{3.15}Sb_{0.5}Bi_{1.4975}Te_{0.0025}$	680	-224	33.22	2.02	210	0.83	157.83	65
$Nb_{0.1}/Mg_3Sb_{1.5}Bi_{0.49}Te_{0.01}$	760	-205	31.64	3	158.5	0.98	154.89	66

Supplementary Table 8.

Output performance testing conditions of f-TEG. Heating element temperature (T_{hot}), circulating water temperature (T_{cold}), and the estimated temperature difference (ΔT) across f-TEG device.

T_{hot} (K)	T_{cold} (K)	ΔT (K)
313	295	1.3
323	295	2.3
333	295	3.3
343	295	4.3
353	295	5.3
363	295	6.3
383	295	7.3

Supplementary References

76. Snyder G. J. & Toberer, E. S. Complex thermoelectric materials. *Nat. Mater.* **7**, 105–114 (2008).

77. Shakouri, A. Recent developments in semiconductor thermoelectric physics and materials. *Annu. Rev. Mater Res.* **41**, 399-431 (2011).